IDŐJÁRÁS

Quarterly Journal of the Hungarian Meteorological Service
Vol. 119, No. 4, October – December, 2015, pp. 443–474

A new hail size forecasting technique by using numerical modeling of hailstorms: A case study in Hungary

Kálmán Csirmaz

Hungarian Meteorological Service Storm Warning Observatory
Vitorlás u. 17. H-8600 Siófok, Hungary
csirmaz.k@met.hu

(Manuscript received in final form March 30, 2015)

Abstract—A new forecasting method for maximum size of hail stones is presented in this paper by using the outputs of a high-resolution, non-hydrostatic numerical weather prediction model (NWP). The method was tested applying simulations of a real case supercell storm producing damaging hail with the Weather, Research and Forecasting (WRF) model. Numerical simulations were made with two distinct horizontal resolutions, 2 km and 100 m, applying nesting technique to assess the effect of the resolution on the storm microphysical properties and the maximum size of the hail stones on the surface. The WRF was able to simulate the main observed characteristics of the supercell on both resolutions. However, the numerical simulation with finer resolution gave better agreement with the radar observation and the observed maximum hail size on the surface. It was found that the horizontal resolution has significant influence on the magnitude and evolution of the microphysical processes in the storm. The numerical simulation with finer resolution produced not only significantly larger maximum mixing ratios of graupel/hail than the 2 km one did, but the volume integrated content of graupel/hail particles in the storm was also larger in the case of finer resolution. This difference can be attributed to the stronger updraft in the case of 100 m resolution. The analysis of various production shows that graupel/hail particles were mainly formed by the heterogeneous freezing of supercooled rain drops and by the freezing of rain drops due to the collision with cloud ice in the midlevels (between 3 and 8 km). Subsequent accretion of graupel/hail particles occurred by the collision with cloud and rain water. Larger graupel/hail content aloft in the case of finer simulation resulted in larger surface mixing ratios which directly led to larger maximum hail sizes on the ground.

Key-words: supercell, hail, WRF

1. Introduction

Hail is a threatening atmospheric phenomenon and storms with hail on the ground (hereafter hailstorms) frequently cause large fraction of weather-related damages. The annual crop losses often reach several hundreds of million dollars (*Changnon et al.,* 2000) in the USA. Hungary is an exposed region, as well: in the 70s, the hail-related annual insurance charges in Baranya county – before the installation of the hail suppression system – totaled to 100–200 million forints. Therefore, prediction of hail on the ground – especially its existence and a characteristic diameter of hailstones –, is a crucial segment of mesoscale forecasts and warning systems. The difficulties of forecasting hail come from the large spatial and temporal variability of hailfalls and relatively low frequency of their occurrence over a certain point of the ground. This makes the verification and validation of any forecasting techniques quite complicated.

The first methods were based on statistical relationships between the observed state of the atmosphere and the existence and size of the hail on the ground (e.g., *Fawbush* and *Miller*, 1953; *Miller*, 1972). From the sixties-seventies, as the capacity of computers had gradually improved, it became possible to explicitly simulate the hail formation and growth in thunderstorms producing hail on the ground. The initial attempts were one-dimensional steady-state "jet" models (e.g., S*impson* and *Wiggert*, 1969; *Weinstein*, 1972; *Zoltán* and *Geresdi*, 1984) and one-dimensional, time-dependent models (*Ogura* and *Takashi*, 1971; *Wisner et al*., 1972; *Ćurić* and *Janc*, 1989 and 1993). Since that time, the statistical methods for forecasting hail have been coupled with one-dimensional cloud models to evaluate the maximum updraft speed (e.g., *Renick* and *Maxwell*, 1977; *Moore* and *Pino*, 1990) or complex microphysics schemes have been combined with simple steady-state cumulus models (e.g., *Brimelow et al*., 2002, *Brimelow* and *Reuter*, 2006; *Geresdi et al*., 2004 etc.). The development of two- or three-dimensional, time-dependent cloud models enabled the more reliable simulations and complex analyses of the microphysical processes and their relationships to the airflow in and around multi- and supercell storms (*Orville* and *Kopp*, 1977; *Takahashi*, 1976; *Johnson et al*., 1993 and 1995; *Geresdi*, 1990 and 1996). However, these models involve bulk microphysics schemes, therefore, they are not able to explicitly compute the evolution of hydrometeor sizes, but only the parameters of their preset size distributions. Though detailed spectral (bin) microphysical models work with size categories, they are computationally more expensive (*Farley* and *Orville,* 1986; *Farley,* 1987 a,b; *Geresdi*, 1998), which inhibits their wide-spread application in multidimensional microphysical numerical experiments and operational application.

Due to the appearance of the new generation of mesoscale, non-hydrostatic models, such as the Weather Research and Forecasting Model (WRF – *Skamarock et al.*, 2008), three-dimensional, real-data simulations of hailstorms became routinely executable in an operational manner via their complex bulk

microphysical schemes. Moreover, using this type of numerical models, explicit prediction of hail or other hydrometeor categories on the ground is also possible. Still, to date, there is barely known any hail forecasting methods based upon the explicit microphysical outputs of mesoscale numerical weather prediction models (NWP). Though *Milbrandt* and *Yau* (2006) developed a method to estimate the maximum size of hailstones at the surface based on the three-moment size distribution of the hail category predicted by NWP, they did not suggest that method as a possible way for operationally forecasting the existence and size of hail stones. In this paper, the description and results of recently developed method about the forecast of the maximum hail size is presented.

The effect of resolution on the morphology of thunderstorms has been thoroughly studied (e.g., *Grabowski et al*., 1998; *Adlerman* and *Droegemeier,* 2002; *Petch et al*., 2002). It was found that the properties of the simulated mesoscale phenomena were very sensitive to the applied horizontal resolution of the model. In relation with this issue, numerous experiments were made to determine the "ideal" resolution to a physically consistent cloud-resolving model regime. *Bryan et al*. (2003), for example, found that a horizontal resolution of about 100 m is necessary for a correct simulation of an idealized squall line case. *Craig* and *Dörnback* (2008) proposed that the horizontal resolution of a consistent mesoscale simulation should be determined by either of horizontal scale of a buoyant bubble or the buoyancy height which requires tens of meters of resolution. *Friori et al*. (2010) examined the effects of resolution and various turbulence schemes on the morphology of a supercell by numerical simulation of idealized cases, and they found the values of storm-scale properties to converge at horizontal resolution of 200 m. To summarize, simulation with horizontal resolution on the order of hundreds of meters is necessary in order to obtain physically as consistent results as possible regarding the microphysical properties of a hailstorm.

Supercells, as effective hail-producing storms, occurs over Hungary every year mainly during the warm season (*Horváth* and *Geresdi*, 2003), and there were successful attempts to simulate them with state-of-the-art NWP's (*Horváth* and *Geresdi*, 2003; *Horváth et. al*., 2009; *Putsay et al*., 2011). However, these studies did not cover the microphysical aspects of the simulations. Therefore, in this paper, a detailed analysis of microphysical processes focusing on the formation and growth of solid hydrometeors (graupel/hail) is given. The analysis was performed, on one hand, on a coarser model grid with *O* (1 km) grid spacing corresponding to the present-day, operationally applied resolution in NWP forecasts and, on the other hand, on a high-resolution domain with *O* (100 m) grid distance which yields physically the most consistent cloud-resolving simulation. The comparison of the storm's microphysical properties on the two distinct grids is also carried out to study the effect of the resolution on the hydrometeor fields in the storm. In Section 2, the methodology of the research and the method for assessing hail-size on the ground are shown. In

Section 3, we describe the details of a case study, and the results of the numerical simulations and hail-size calculations are presented. Summary and plans for future work are given in Section 4.

2. Methodology

2.1. Description of the modeling environment

The simulations were carried out with the WRF-ARW non-hydrostatic mesoscale numerical model version 3.1.1 (*Skamarock et al*., 2008) using nested domains with different horizontal resolutions. The largest domain (Domain 1) has a resolution of 6 km and it covers an area of 700 km × 850 km in the Carpathian Basin. The second, smaller domain (Nest 1) includes Hungary, too, but it has 2 km resolution and covers a region of 450 km × 360 km. The smallest domain (Nest 2) is embedded in Nest 1. This domain is used to focus on the particular storm, therefore its horizontal resolution is 100 m and covers only an area of 44 km × 30 km. This resolution was chosen according to the results published by *Bryan et al.* (2003). They found that – in the case of idealized boundary conditions – the simulated properties of a squall line showed convergence if the horizontal resolution was equal to or less than 100 m. This means that the further decrease of horizontal grid distances hardly affects the output of the numerical model. It is supposed that the above-mentioned conclusion of *Bryan et al.* (2003) is valid for the supercell case presented in this paper, too. The vertical resolution was the same in each nest: 37 terrain-following levels were applied with larger vertical resolution near to the surface and with stretched resolution at higher altitudes. The lowest model level was about ten meters above the ground and the top of the domain was at 50 hPa. All in all, we performed one model run on three domains (Domain 1, Nest 1 and Nest 2) connected via one-way nesting technique, but only the results on Nest 1 and Nest 2 were evaluated. We consider the model run on Nest 1 and Nest 2 as distinct simulations, therefore, hereafter we are referring to these simulations as Simulation1 (Nest 1) and Simulation2 (Nest 2). See *Fig. 1* for the location of domains of the simulations.

The formation and evolution of different types of hydrometeor species was simulated by the Thompson's one-moment bulk microphysical scheme (*Thompson et al*., 2004) adapted from the Reisner scheme (*Reisner et al*., 1998). The Thompson's parametrization is a state-of-the-art Simulation of the microphysical processes, especially in the case of mixed phase clouds. This scheme allows us to study the characteristics of different types of ice particles in severe thunderstorms. The scheme involves prognostic equations of mixing ratios for five different species: cloud water, cloud ice (cloud particles), snow, rain, and graupel/hail (precipitation particles). The parametrization does not include hail as a distinct category but larger graupel particles computed implicitly by the model can be

treated as hailstones[1]. Grell's cumulus parameterization scheme (*Grell* and *Dévényi*, 2002) is used to simulate the formation of convective clouds. In the cases of larger resolution (i.e., Simulation1 and Simulation2), this parameterization scheme was switched off and the model was let to develop the convection directly. Independently of the horizontal resolution, the Mellor-Yamada-Janjic's (MYJ – *Mellor* and *Yamada*, 1982) planetary boundary layer (PBL) parametrization scheme is activated coupled horizontally with Smagorinsky's first order closure treatment for the sub-grid diffusion. A proper selection from the schemes describing the turbulence is crucial. The main problem about the choosing of the appropriate scheme is that different resolutions need different treatments of the turbulence. As the horizontal resolution is increased from 2 km to 100 m, the averaged momentum equations of the model begin to resolve the boundary layer eddies (large eddy simulation – hereafter LES). This range of resolution is named "terra incongnita" by *Wyngaard* (2004). Eddies in this size interval possess the main fraction of the turbulent energy spectrum regarding cumulus convection. Nevertheless, a Simulation in "terra incongnita" is not able to adequately resolve the energy-containing eddies based on subgrid diffusion closure with a scalar diffusivity. Instead, *Wyngaard* (2004) suggested that a tenzor of three-dimension scalar diffusivity coefficients should be applied in such Simulations. In addition, for a nested, real data case simulated by WRF, *Talbot et al.* (2012) showed that applying LES in "terra incognita" yielded mixed results in the model performance. In addition, they found that the results on the nest with ultra-fine resolution (on the order of 100 m's) were even more sensitive to the lateral boundary conditions and to the initial forcing (represented by the analysis) than to the chosen turbulence closure. These are the reason why the same schemes – the MYL-scheme for handling the vertical diffusion and the Smagorinsky first order scheme for parameterization of the horizontal eddy diffusivity coefficients – were used both in the case of Simulation1 and Simulation2.

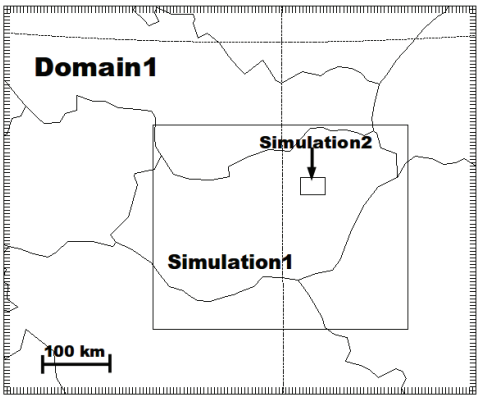

Fig. 1. Location of Domain1 and the nests of Simulation1 and Simulation2 in the WRF model run.

1 In this case, implicit means that the scheme only returns with the mixing ratio of graupel/hail in a grid box. However, upon this quantity and the size distribution, hypothetical and possible particle sizes with their concentration can be assessed.

Initial and lateral boundary conditions for Domain 1, Nest 1, and Nest 2 were provided by the ECMWF global model, by the outputs of Domain 1, and by the outputs of Nest 1, respectively. (The WRF model outputs were generated in every 5 minutes in the case of Simulation1, and in every 1 minute both in Simulation2 and Simulation1 during the time interval when the storm was in the volume defined by Nest 1. Analyses and hail-size calculations were performed on the model's terrain-following eta-system. For the plotting of vertical cross sections, the data were transformed into a Cartesian system with height above the mean sea level as a vertical coordinate.

2.2. Description of the data collected for validation

The results of the numerical model and that of the recently developed hail size forecasting method are intended to compare with observation data. The reliability of the forecast of maximum hail size depends both on the quality of the model output and on the accuracy of the method used on the calculation of the maximum hail size from the model output. Therefore, for the validation of the forecast of maximum hail stone size, such a case was chosen where the model was able to simulate the characteristics of a severe storm correctly, and surface observation data about the size of the hail stones were available. Database of well-documented cases of severe hailstorms was searched to find the appropriate case. This means that, besides the data of hail existence, data on the hailstone sizes should be also available. In the eighties a hail pad network operated in the southern parts of Hungary associated with the hail suppression activity. Unfortunately, this type of hail size measurements was ceased in the early 90's. Since then, there have been no directly observed, quantitative data about the hailstone sizes on the surface, but only qualitative and indirectly observed data about the characteristics of the hailstones are available. The source of data is the followings: 1) Online sources of falling hailstones on various commercial and amateur meteorological sites where extensive documentation of significant severe weather events can be found. These documentations were done mostly by voluntary people who uploaded their photos and videos of hailstones to these sites. These sources, though to a limited extent, can be used for verification. 2) Radar observation data which are not suitable for direct evaluation of hailstone sizes at the ground due to the uncertain relation between the observed reflectivity and hail stone size. However, high reflectivity itself can indicate the existence of hail or perhaps severe hail. Therefore, comparison between the measured and simulated reflectivity is also performed in order to evaluate the model's ability to reproduce the microphysical characteristics of real storms. The simulated radar intensity was calculated by the NCAR Command Language (NCL) post-processing module of WRF-ARW.

2.3. Description of the hail-size calculation method

Forecasting of maximum hail-size is based on the followings: the model computes the graupel/hail mixing ratios on the three-dimensional model grid at every time step. These calculations are carried out by taking the size following gamma size distribution of graupel/hail particles (*Fig. 2*) defined by the scheme (see *Thompson et al.*, 2004) at the lowest model level ($\eta = 0.997$):

$$N(D) = N_0 D e^{-\lambda D}, \tag{1}$$

where D is the diameter of graupel/hail particles (they are supposed to be spherical objects). T

$$N_0 = 2.38\left[\frac{\pi\rho_g}{q\rho_a}\right]^{0.92}, \tag{2}$$

where is ρ_g the density of a graupel/hail particle (400 kgm^{-3}) and ρ_a is the density of air.

The λ parameter can be obtained from the mixing ratio via the following relationship:

$$q = \frac{1}{\rho_a}\int_0^\infty N_0 \frac{D^3\pi}{6}\rho_g D e^{-\lambda D} dD \tag{3}$$

After calculating the integral on the right hand side of Eq. (3), the λ parameter can be given in an explicit form:

$$\lambda = \left[\frac{4N_0\pi\rho_g}{q\rho_a}\right]^{0.2}. \tag{4}$$

The number concentration of graupel/hail particles can be computed via the following equation:

$$n = \int_0^\infty N_0 D e^{-\lambda D} dD = \frac{N_0}{\lambda^2}. \tag{5}$$

A definite integral of Eq. (5) between X and ∞ gives the number concentration of particles larger than X. The algorithm of hail size forecast is based on the following equation:

$$n_X = \int_X^{\infty} N_0 D e^{-\lambda D} dD = N_0 \frac{e^{-\lambda X}}{\lambda^2} (\lambda X + 1) , \quad (6)$$

where n_x is a predefined threshold number concentration of graupel/hail particles. The Newton-Raphson iteration technique was used to calculate the value of the variable X, the diameter of graupel/hail particles which concentration is equal to n_x. The value of this threshold number concentration was chosen to be equal to 10^{-4} m^{-3} (*Milbrandt* and *Yau*, 2006). This value means that there is exactly one hail stone in a volume of column with height of 1 m and with cross section of 100 m × 100 m^2. The hail stones of lower concentration than the threshold are very difficult to detect. Therefore, X can be defined as maximum observable (possible) hail size.

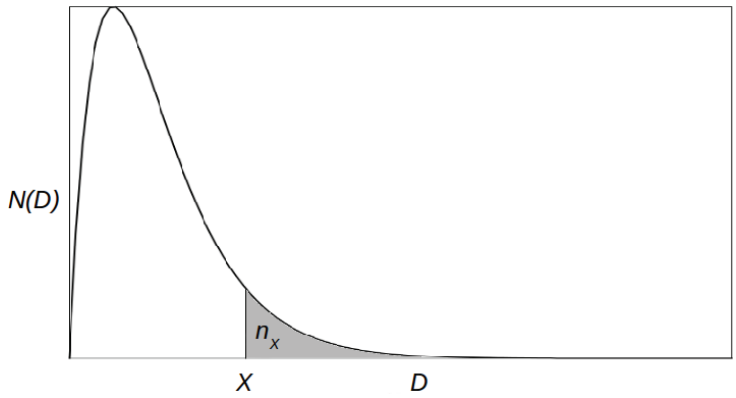

Fig. 2. The gamma distribution of graupel/hail particles used in the Thompson's scheme. *D* on the abscissa represents the graupel diameter, *N(D)*dD* along the *y*-axis is the number concentration of graupel in the infinitesimal *D, D+dD* interval. *X* denotes the diameter above which the concentration is equal to n_x. See text for further description.

3. Results

3.1. Case study: synoptic features and observation data

On June 7, 2009, an isolated supercell passed through the northeastern part of Hungary, produced large hail (the maximum hail stone diameter was reported to be about the size of a tennis ball) causing severe hail-related damages in several locations. The synoptic feature of this event was characterized by a quasi-stationary waving cold front at northwest of Hungary (*Fig. 3a*). East of the front, over Hungary, warm and moist air advected from the south at low-levels. At upper-levels, at the western part of Hungary, the front is accompanied by a trough (not shown) moving slowly eastward. Downstream of the trough, high

wind speeds prevailed aloft (~30 m/s at 500 hPa). These conditions resulted in considerable instability and significant vertical wind shear: ~1000 J/kg convective available potential energy values and 25–30 m/s as magnitudes of vector differences between winds at the surface and 6 km (*Fig. 3b*). These parameters are good indicators regarding the large chance of developing supercells (*Thompson et al*., 2003).

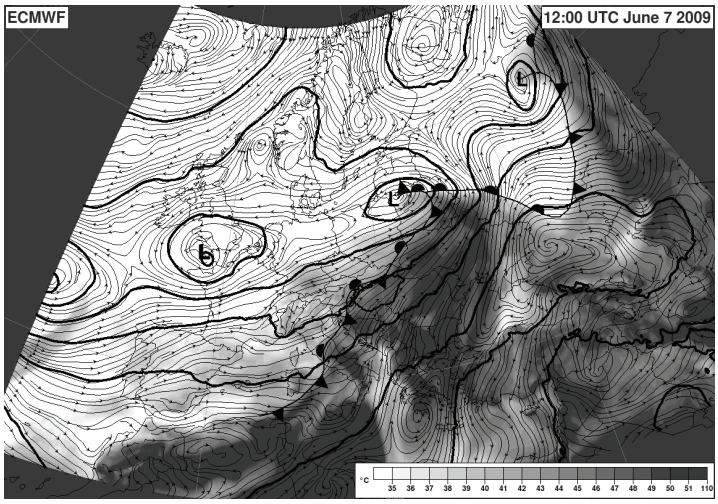

Fig. 3a. The synoptic situation of the waving front over Central Europe at 12:00 UTC, on June 7, 2009 according to the ECWMF analysis. Shading represents the equivalent potential temperature field (in Celsius) at 850 hPa, black solid lines denote the geopotential height of the 850 hPa pressure level (contoured with 40 m intervals), streamlines denote the wind at 850 hPa. Letter L denotes low heights (low pressures).

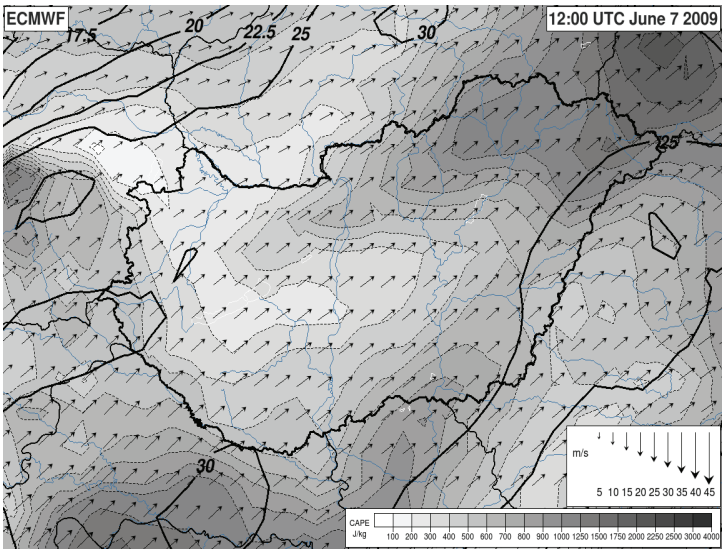

Fig. 3b. Convective available potential energy (shaded), 0–6 km vertical wind shear (magnitude of the vector difference, m/s, solid black lines), and 0–6 km mean wind (black arrows) at 12:00 UTC, on June 7, 2009 above Hungary according to the ECWMF 12:00 UTC analysis.

According to composite radar images generated in every 15th minute, the supercell developed at 12:30 UTC over the central part of Hungary, then rapidly propagated (with an average speed of 75 km/h) northeastward, passed north of Nyíregyháza, left the country at 14:30 UTC, and dissipated at 16:30 UTC in Ukraine. Thus, its lifetime reached three and a half hours. The reflectivity inside the hail storm reached its maximum value of 67.5 dBz at 13:45 UTC (*Fig. 4*). Based on news reports, the cell caused the most hail-related damages along the line of Tiszavasvári-Nyírszőlős-Kemecse-Nyírbogdány-Demecser-Berkesz villages (see their location in *Fig. 4*). Voluntary observers reported maximum hailstone size of around 4 cm (*Fig. 5*).

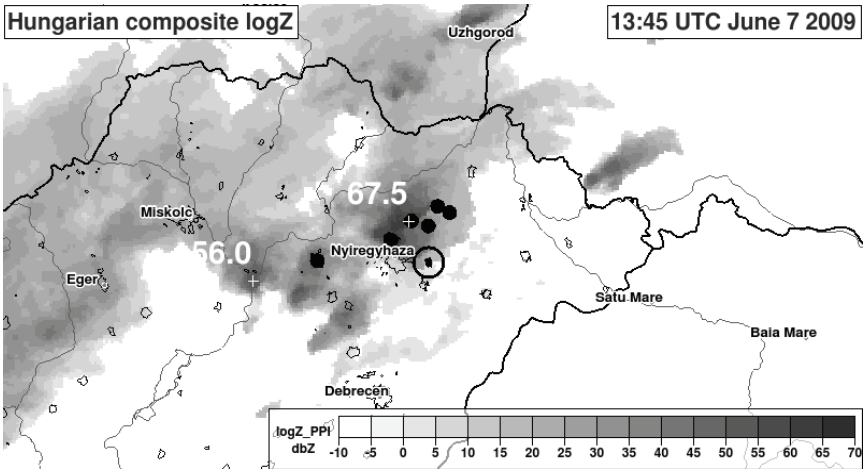

Fig. 4. Observed radar picture of the simulated thunderstorm at 13:45 UTC, on June 7, 2009. Shading represents the intensity in dBz, which is the column maximum reflectivity. Maximum values are indicated by white numbers. Villages exposed to large, damaging hail are denoted by dots. The location of the closest radar site (Napkor) is depicted by a black circle. The direction of propagation of the storm is denoted by a black arrow.

Fig. 5. Observed typical hail sizes in the villages (see text) crossed by the supercell on June 7, 2009. (Source: idokep.hu)

Analysis of reflectivity and radial velocity data proved that the hailstorm was a supercell with considerable rotational features. The storm moved along slightly north to the location of the radar at Napkor, east of Nyíregyháza (as seen in *Fig. 4*). According to the results of the analysis of Doppler radar data (*Fig. 6*), the storm did not showed features of low-level rotation in its development phase (from its formation at around 12:30 UTC to 14:30 UTC). However, considerable midlevel vortex (not shown) and, as a sign of highly sheared environment, a significant weak-echo region (WER) with high-reflectivity regions aloft on its downshear (to the east) side (not shown) were detected. After the storm passed Napkor, between 13:45 and 14:00 UTC, a well-visible hook echo feature developed on its southern side accompanied by a bounded weak echo region (BWER), and a vault extended on its downshear flank. At the same time, a low-level vortex (depicted by a rectangle in *Fig. 6*) formed around the hook echo region. According to *Lemon* and *Doswell* (1979), these features suggest that the hailstorm – during the long period of its lifetime – behaved as a supercell storm.

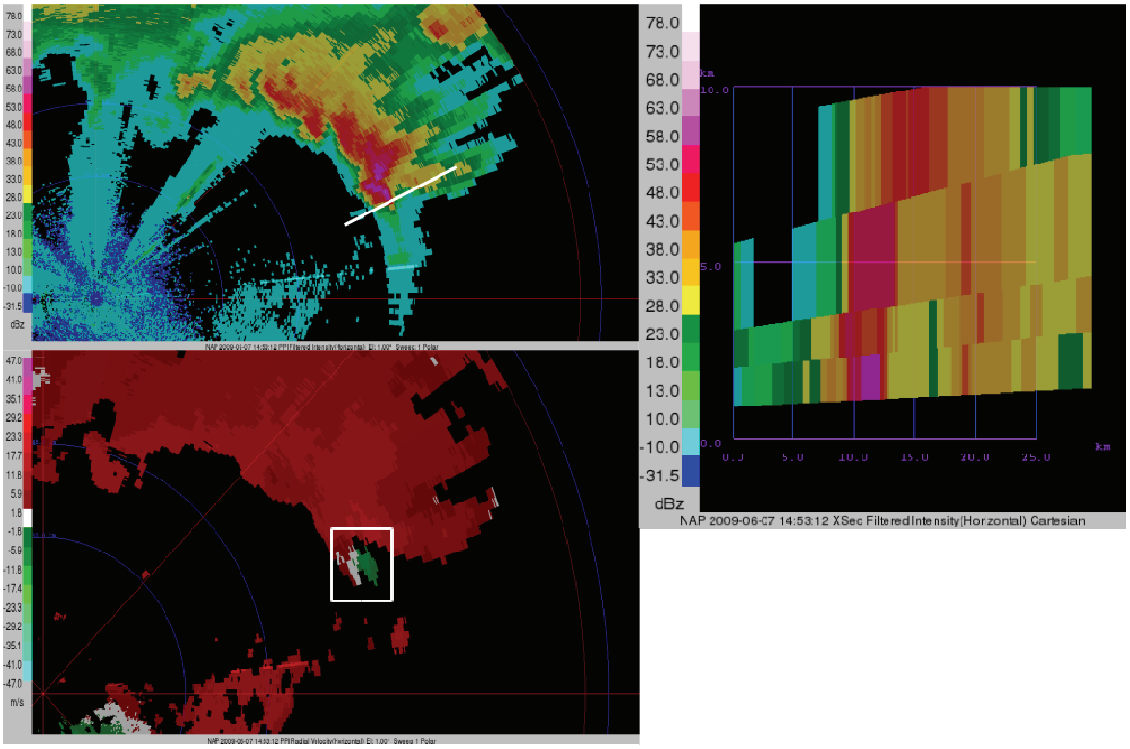

Fig. 6. PPI reflectivity (upper left), storm-relative radial velocity (lower left) at an elevation angle of 1 degree and vertical cross section of reflectivity (right) through the storm observed by the Napkor radar at 14:53 UTC, on June 7, 2009. Circles in the pictures on the left depict distances of 30 km, 48 km, and 115 km from the radar. The white line in the PPI denotes the orientation of the cross-section on the right. In the radial wind picture, red colors indicate approach, greenish colors mean drawing-away. The rectangle on the left lower picture encloses the area of significant radial shear, i. e., the location of a mesocyclone which has an altitude of around 1 km.

3.2. Results of numerical Simulation

The Simulations of WRF were initialized at 06:00 UTC, June 7, 2009 from the 00:00 UTC, June 7, 2009 ECMWF run, and was run until 18:00 UTC, June 7, 2009. The finest, 100 m grid (Simulation2) extended to a 44 km × 30 km area (440 × 300 horizontal grid points) was located in the path of storm formed in Simulation1.

3.2.1. Verification

The simulated reflectivity data on both grids at a given time are shown in *Fig. 7*. The reflectivity structure of the simulated thunderstorm is similar to that of the observed one (*Fig. 4*): an isolated high-reflectivity core with a significant gradient at the southern part of the cell and a much smoother gradient downstream with an accompanying larger scale weak-reflectivity pattern can be observed both in *Fig. 4*. and *Fig. 7*. These features indicate the presence of a supercell with rotating mesocyclone in a highly sheared environment.

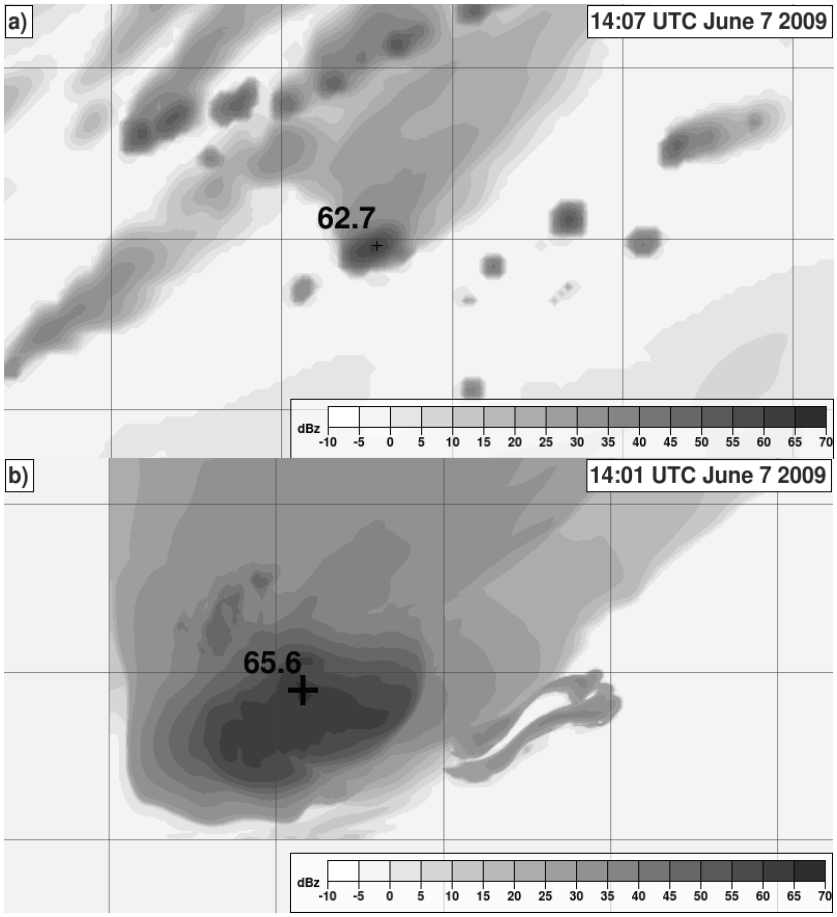

Fig. 7. Calculated column-maximum reflectivity in dBz a) in Simulation1 at 14:07 UTC and b) in Simulation2 at 14:01 UTC, June 7, 2009. The numbers denote the maximum values. The square boxes represent 25 km × 25 km and 10 km × 10 km areas in a) and in b), respectively.

Time evolution of both simulated and observed maximum values of reflectivity can be seen in *Fig. 8a*, which shows that Simulation1 underestimated the intensity of the cell throughout its lifetime. In the case of Simulation2, the cell entered Nest 2 has a maximum reflectivity of 62 dBz, and five minutes later it reached 66 dBz. These values are much closer to the observed ones than the simulated reflectivity values in the case of Simulation1. Note, that data for this high reflectivity core are only available between 13:45 and 14:30 UTC in Simulation2, because Nest 2 was rather small (only 44 km × 30 km), and the fast-moving cell (at a speed of about 55 km/h) quickly passed it.

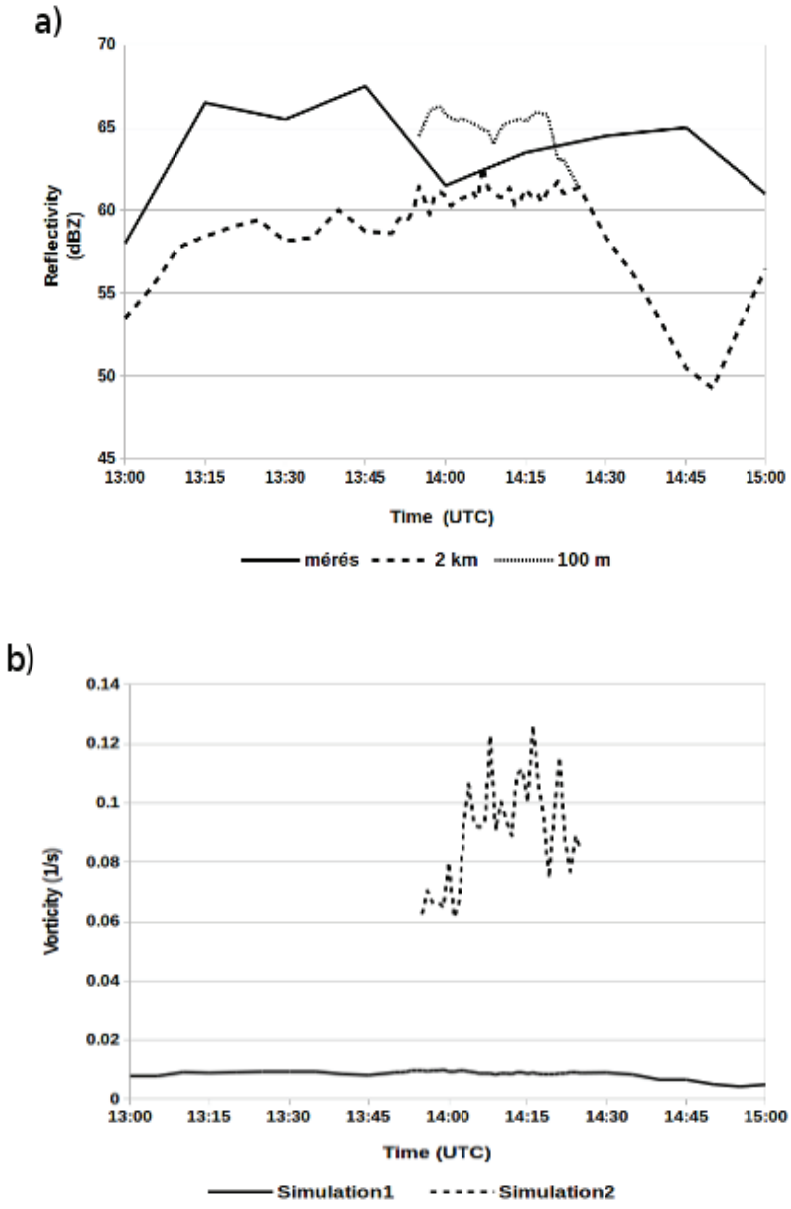

Fig. 8. Time evolution of a) the observed and simulated maximum reflectivities and b) the maximum relative vertical vorticity in the supercell in the case of Simulation1 and Simulation2 on June 7, 2009.

In order to assess the model's capability of simulating the dynamics and related structures of the supercell, spatial and temporal evolution of the vertical vorticity field were also investigated. *Fig. 8b* shows the time evolution of maximum midlevel (between 3 and 7 km) vertical vorticities. In the case of Simulation1, the maximum vertical vorticity remains near to 0.01 1/s (or slightly below). On the other hand, the supercell in Simulation2 developed a much more intense vortex with values larger than 0.06 1/s (for a short time even larger than 0.1 1/s). Horizontal cross-sections of vertical vorticity field around the simulated cell at a certain time step, together with other ultimate parameters, are plotted in *Fig. 9*. The cross sections are given at the height of 5 km, thus they characterize the midlevel structure of the storm. In the case of Simulation1 (*Fig. 9a*), an area of a strong updraft with vertical velocities between 20 and 30 m/s is coupled with moderately strong positive vertical vorticity in such a way, that the maximum of vertical vorticity lies on the right flank of maximum updraft velocities. This configuration corresponds well with both the observational (*Lemon* and *Doswell*, 1979) and simulated (*Klemp*, 1987) structures of supercells. The intensity of vertical vorticity hardly reaches the value of 0.01 1/s, which is a threshold for the formation of a mesocyclone (*Doswell*, 1996). The accompanying storm-relative streamlines show no pure vortices (the streamlines are curved but not enclosed). However, the areas of downdraft (indicated by the rainwater at the surface) and the updraft are horizontally well separated, which is a necessary condition for long-lived thunderstorms (*Browning*, 1968). Similar structure developed in the case of Simulation2 (*Fig. 9b*). The features are more obvious than in the case of Simulation1. The vertical vorticity is more intense (with maximum value of 0.05 1/s); the closing streamlines depict a true cyclonic vortex to the right of the updraft and a pure anticyclonic vortex deep in the precipitation zone; and the surface rain mixing ratio is much higher (above 10 g/kg), as well. It can be concluded that both Simulations were able to catch the essential structure of supercell, but the Simulation with finer resolution generated a cell with much more expressed features.

3.2.2. Comparison and evaluation of microphysical properties and production terms of graupel/hail of Simulation1 and Simulation2

The time evolution of maximum in-storm values of mixing ratios of all hydrometeor categories (cloud water, cloud ice, rain, snow, and graupel/hail) in Simulation1 and Simulation2 are plotted in *Figs. 10a* and *b*. The spatial resolution seems to have a significant effect on the amount of the precipitation particles. The simulation with finer resolution produced larger maximum mixing ratios of graupel/hail particles and that of rain water (*Fig. 10a*). The mean maximum mixing ratios of these precipitation species are 3–4 g/kg and 5–7 g/kg higher in the case of Simulation2 than in the case of Simulation1. No significant differences were found in the case of maximum mixing ratio of the snow. If we

assess the differences in cloud particle mass (cloud water and ice) and relative humidity maximum between the two resolutions (*Fig. 10b*), then the following conclusions can be drawn: while Simulation1 and Simulation2 give similar maximum cloud water mixing ratios (~2–4 g/kg), the maximum value of cloud ice mixing ratio is significantly larger in the case of Simulation1, than in Simulation2 (~0.4–0.6 g/kg versus ~0.2 g/kg). The obtained in-cloud (above 3km) maximum water vapor mixing ratio was about 6–7 g/kg on both grids with a bit higher value on the 100 m resolution grid.

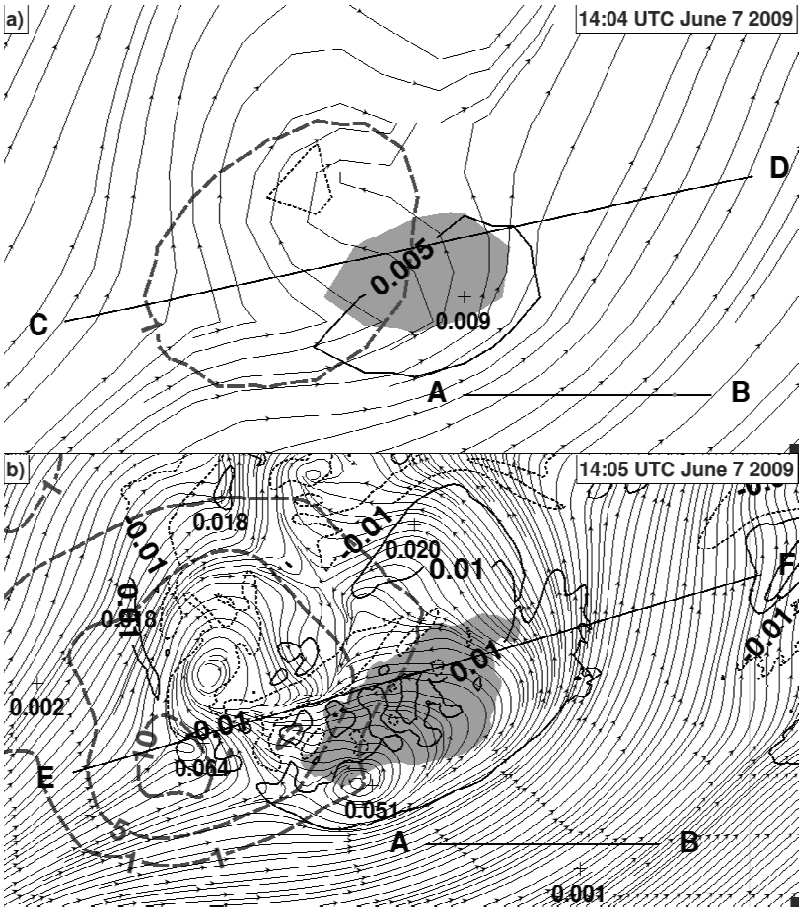

Fig. 9. Simulated horizontal, storm-relative streamlines; relative vertical vorticity (light solid contour of positive values; light dashed contours of negative values); vertical velocity (grey shaded area above the value of 20 m/s) at z=5 km, and rainwater mixing ratio (dark grey bold dashed contours of 1, 5, and 10 g/kg) at z=50 m.
a) in Simulation1 at 14:04 UTC on, June 7, 2009. As for vertical vorticity, only the 0.005 1/s and –0.005 1/s isolines are shown. The length of AB line is 10 km. The CD line represents the horizontal orientation of the vertical cross section in *Figs. 13a* and *b*, and *Figs. 14a* and *b*.
b) in Simulation2 at 1405 UTC on, June 7, 2009. As for vertical vorticity, only the 0.01 1/s and –0.01 1/s isolines are shown. The length of AB line is 2,5 km. The EF line represents the horizontal orientation of the vertical cross section in *Figs. 13c* and *d*, and *Figs. 14c* and *d*.
In both pictures, the local maximum values of vertical vorticity (1/s) are indicated by numbers.

The microphysical processes regarding the formation of graupel/hail in the cloud were analyzed by plotting the time evolution of the production terms of graupel/hail mass. The following production terms are included in the Tompson's scheme (without the melting): deposition/sublimation of water vapor onto/from the graupel/hail surface (gde), conversion of snow into graupel/hail due to riming (sgc), freezing of supercooled rainwater (frz), collision of rainwater and snow (rcs), collection/accretion of graupel/hail by cloud water (gcw), collision of rainwater and graupel/hail (rcg), freezing of rainwater by its collision with cloud ice (rci), and graupel/hail production due to ice multiplication during riming process (ihm) (*Hallet* and *Mossop*, 1974). These production terms were averaged around the location of the maximum mixing ratio of graupel/hail in a volume, which involves 3×3 (in Simulation1) and 60×60 (in Simulation2) grid points horizontally (each represents a $6\,\text{km} \times 6$ km square) and 3 grid points vertically (in both simulations). Note, that results of Simulation2 are plotted only between 13:55 and 14:25 UTC because this was the time period when the cell stayed inside of Nest 2.

Time evolution of the production terms in *Figs. 10c* and *d* show that the larger amount of graupel/hail in the case of Simulation2 is the consequence of the considerably larger freezing rate of rainwater (the difference between Simulation2 and Simulation1 is about an order of one magnitude). Subsequently, the amount of graupel/hail further increased due to the more efficient accretion by supercooled cloud water drops (this latter production term is two times larger in Simulation2 than in Simulation1). The riming of cloud ice by cloud water acts as a strong sink of cloud ice (much more efficient than cloud ice-rain collision). Because the formation of snow is more efficient due this process in Simulation2 than in Simulation1 (not shown), more cloud ice particles remain in the latter case. As a consequence, the graupel/hail production due to rain-ice collision is significantly larger in Simulation1 than in Simulation2. The height of maximum graupel/hail mixing ratio is larger in Simulation2 than in Simulation2 during the first half of the 13:55–14:25 UTC time period (slightly below 7 km in Simulation1 and between 7–8 km in Simulation2). After this time period, it rapidly decreases below 5 km in Simulation2 (in Simulation1 the decrease is gradual).The larger height of maximum in Simulation2 can be attributed to the larger vertical velocities (see next paragraph), which can transport the graupel/hail mass to higher altitudes.

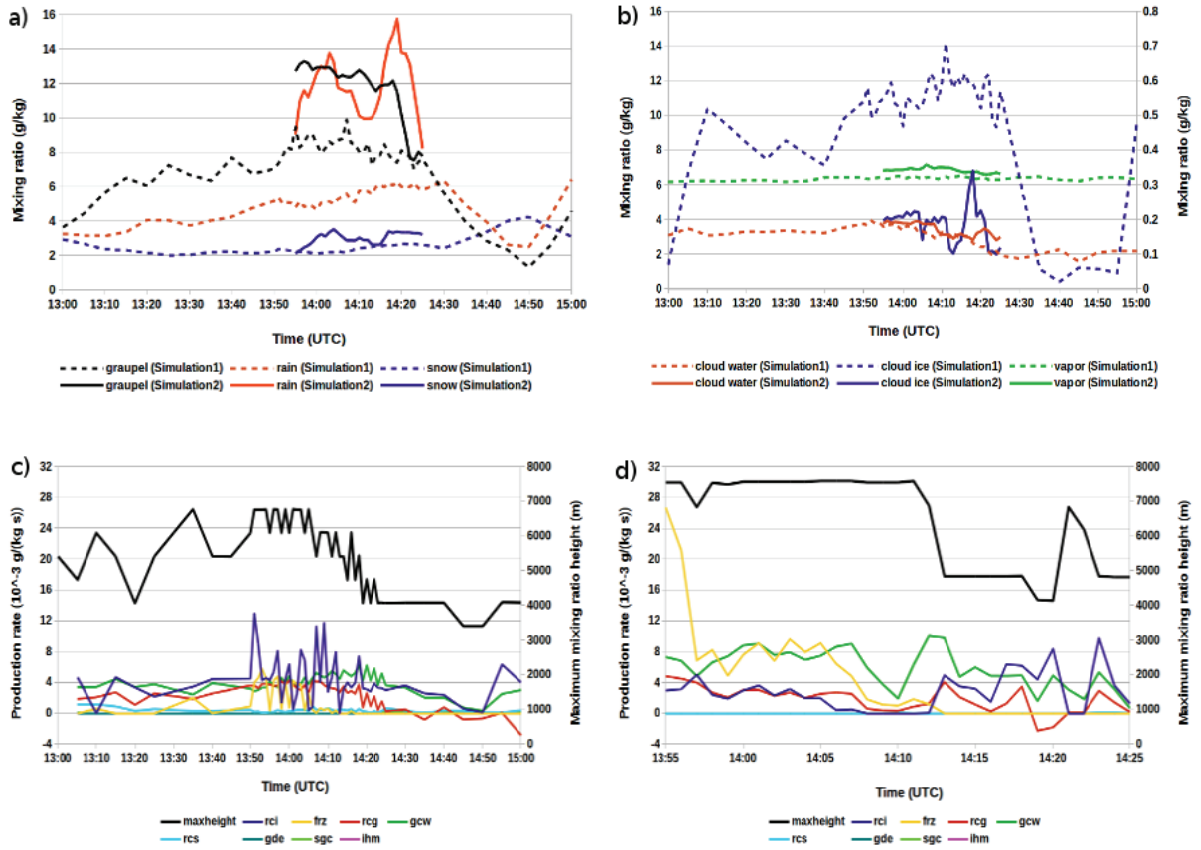

Fig. 10. Time evolution of maximum in-storm values of a) precipitation particles (graupel, rain, and snow in g/kg), b) cloud particle mixing ratios (g/kg) of both nests. c) and d) shows the tendency of graupel production terms (in mg/kg s) averaged around the maximum graupel mixing ratio (see text) in Simulation1 and Simulation2, respectively. For the description of abbreviations in the legend of c) and d) see text. Curve maxheight represents the height (above ground level) of the maximum graupel mixing ratio.

Maximum of updraft and downdraft velocities in the vicinity of the maximum mixing ratio of graupel/hail and the time evolution of maximum graupel/hail mixing ratio on the surface are plotted in *Fig. 11*. In the case of the updraft, vicinity means that the maximum values are chosen from a volume contains $3 \times 3 \times 5$ and $11 \times 11 \times 5$ grid points around the location of the graupel/hail maximum in Simulation1 and Simulation2, respectively. The maximum value of downdraft was taken from a volume contains the location of maximum graupel/hail mixing ratio on the surface. The bottom of this volume is on the surface, its horizontal extension is the same as it was mentioned above. The depth of the volume is 6 km. The maximum vertical velocity was larger in the case of Simulation2 (peaked at around 35 m/s) than in Simulation1 (below 30 m/s, around 25 m/s) almost all the time during the simulation. This difference could explain why maximum graupel/hail mixing ratios aloft is greater in Simulation2. The stronger updraft could hold up larger amount of graupel/hail

aloft, and the larger vertical velocity might resulted in larger upward vapor flux, which subsequently could promote the enhanced production of rainwater and graupel/hail. Furthermore, due to larger condensation rate, more latent heat is released which could further intensify the updraft. The strong relation between the updraft intensity and the maximum mixing ratios of precipitation particles aloft is clearly visible by comparing the plots in *Fig. 11* and *Fig. 10a*. These figures show that the time evolution of the maximum of mixing ratios (both rain and graupel/hail) and maximum of updraft velocities run parallel. On the surface, the maximum of graupel/hail mixing ratio is considerably larger in Simulation2 than in Simulation1. Sometimes this difference is as large as one order of magnitude (~2–3 g/kg in Simulation2 and 0.3–0.6 g/kg in Simulation1). This is the consequence of the larger maximum mixing ratio of graupel/hail aloft in Simulation2. The larger amount of graupel/hail aloft generates stronger downdraft by loading, evaporative cooling, and melting effects. This is the reason why stronger downdraft developed in the case of Simulation2 than in the case of Simulation1 (~10–15 m/s versus ~5 m/s).

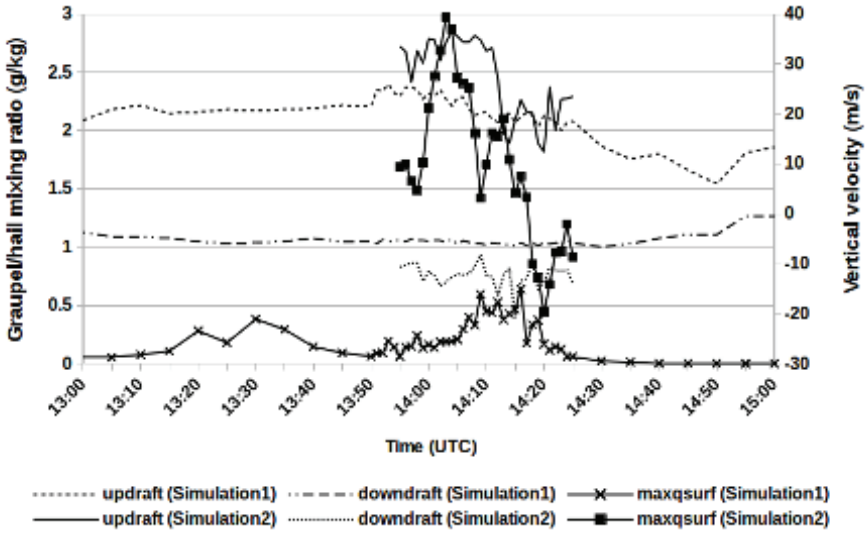

Fig. 11. Time evolution of maximum updrafts and downdrafts (m/s) and the mixing ratios of graupel particles at the lowest model level (g/kg) in the simulated cells in both cases.

It is important to clarify, whether these above mentioned differences between the results of Simulation1 and Simulation2 on the surface are valid also for the volume integrated values of graupel/hail mixing ratios, or they represent the differences only for the maximum values. This problem is critical if the amount of the hail on surfaces is intended to be forecast. Time evolutions of graupel/hail mixing ratios integrated over a square of 196 km^2 are plotted in *Fig. 12*. The location of the center of this square is fitted to the grid point where the mixing ratio of the graupel/hail has maximum value on the surface. *Fig. 12*

also shows the time evolution of the extent of the region where the graupel/hail mixing ratio exceeded 0.001 g/kg on the surface. The comparison of the curves shows, that not only the maximum graupel/hail mixing ratio is larger in Simulation2, but the total amount of graupel/hail mass is also significantly greater. In the case of the areas where the mixing ratio of the graupel/hail is larger than 1 mg/kg, the difference between the two Simulations is not significant, yet Simulation1 gives larger area during a relatively long time period.

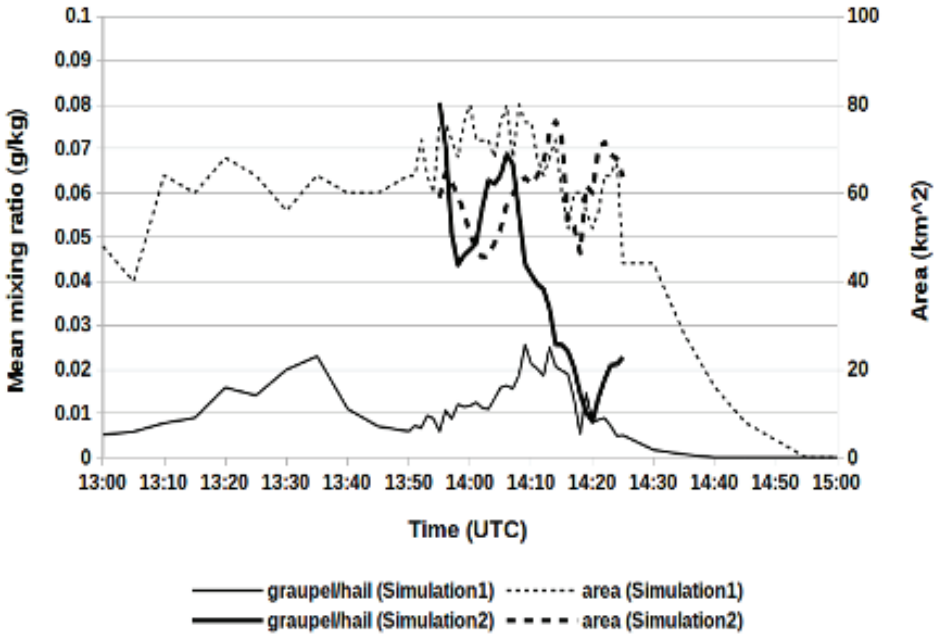

Fig. 12. Time evolution of mean values of graupel particle mixing ratios (g/kg) and the area of graupel mixing ratios above 0.001 g/kg (km^2) at the lowest model level in the simulated cells in both nests for the June 7, 2009 case.

The influence of the spatial resolution on the microphysical properties of the simulated thunderstorm is shown by vertical cross sections of the storm. *Figs. 13a-d* show the cross section calculated in Simulation1 and in Simulation2, respectively. The morphology of the thunderstorm is clearly visible in the case of both resolutions: (i) the horizontally separated updraft and downdraft regions; the rearward tilted updraft region; (ii) the mid-level maximum of the graupel/hail mixing ratios at mid-level; (iii) the WER (in Simulation2, even a slight BWER structure visible at $z = 4$ km – see *Fig. 13d*) at low altitudes due to the intense updraft; (iv) the fall-out of graupel/hail and rain in the rear side of downdraft; (v) the downwind advection of the graupel/hail, snow, and cloud ice (right side of the cross sections) aloft forming an anvil-like structure.

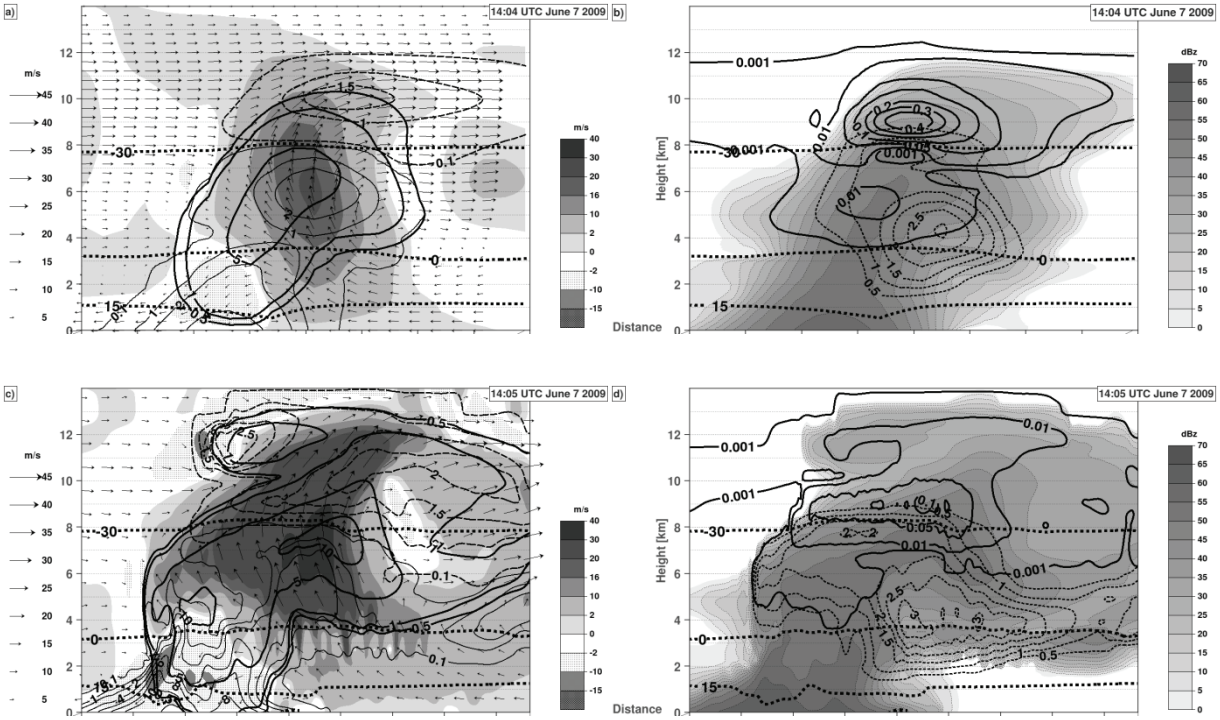

Fig. 13. Vertical cross sections of the thunderstorm in Simulation1 at 14:04 UTC and in Simulation2 at 14:05 UTC on June 7, 2009. The vertical dimension is in km unit. Cross sections in a) and b) were created by Simulation1 and marked by the CD line in *Fig. 9a*. Cross sections in c) and d) were created by Simulation2 and marked by the EF line in *Fig. 9b*. The displayed quantities are the followings:
a) and c): vertical wind speed (shaded), storm-relative streamlines in the plane of the cross section (arrows), graupel mixing ratio (thick solid contours of 0.5, 1, 5, 7.5, 10 g/kg and above 10 g/kg with intervals of 5 g/kg), rainwater mixing ratio (light solid contours of 0.1, 1, and 2 g/kg and above 2 g/kg with intervals of 2 g/kg), and snow mixing ratio (light dashed contours of 0.1, 1 g/kg and above 1 g/kg with intervals of 0.5 g/kg). Thick dashed lines denote the isolines of 15, 0, and –30 °C.
b) and d): simulated radar reflectivity (dBz units), cloud ice mixing ratio (thick solid contours of 0.001, 0.01, and 0.05 g/kg, 0.1 g/kg, and above 0.1 g/kg with intervals of 0.1 g/kg), cloud water mixing ratio (dashed light contours with intervals of 0.5 g/kg), and the isolines of the 0 and –30 °C temperatures (dashed thick contours). Thick dashed lines denote the isolines of 15, 0, and –30 °C.

Nevertheless, the differences between the two cases are also apparent. The updraft intensity in the case of finer resolution is much greater than on the coarser grid (30–40 m/s maximum of updraft velocity in Simulation2 versus 20–30 m/s in Simulation1). The differences in the cloud dynamics correspond to the height of the cloud top. It is about 14 km in the case of Simulation2 and around 12 km in the case of Simulation1 (the cloud ice isoline of 1 mg/kg is defined as an upper boundary of the cloud). The maximum of graupel/hail mixing ratio is between 10–15 g/kg and between 7.5–10 g/kg in Simulation2 (*Fig. 13c*) and in Simulation1 (*Fig. 13a*), respectively. The altitudes of the maximum of graupel/hail mixing ratio are also different in the two cases (~7–8 km versus ~6–

7 km). The mixing ratio of graupel/hail particles on the surface is an important characteristic of the morphology, too. While the isoline of 1 g/kg graupel/hail mixing ratio reaches the surface in Simulation2, even the bottom of the isoline of 0.5 g/kg is above the surface in the case of Simulation1. This means that – in agreements with the previous findings upon the time evolutions in *Fig. 11*, the fine-resolution storm produced considerably greater graupel/hail mixing ratio values on the surface than its coarse-resolution counterpart does. This result has consequences on the the maximum possible hail-size (see Section 3.2.3. for details). In both cases, the location of maximum of graupel/hail mixing ratio mass is in spatial correlation with the maximum of updraft velocity. The significant rearward advection of graupel/hail and rain results in rear-flank downdraft and mixed phase precipitation on the surface (*Figs. 13a* and *c*). The amount of the rain on the surface is almost twice larger in Simulation2 than in Simulation1 (9–10 g/kg versus 4–5 g/kg). Similarly to the previous findings, the high-resolution storm in Simulation2 produced larger simulated radar intensity (*Figs. 13b* and *d*) than in Simulation2 (above 60 dBz versus below 60 dB). It is a remarkable feature that the maximum radar reflectivity is at low-levels in both Simulations which can be attributed to the melting graupel/hail inducing great reflectivity. Considering the isolines of cloud water mixing ratio (*Figs. 13b* and *d*), their structures and maximum values are very similar (~3 g/kg). However, while in Simulation2, the isoline of 1.5 g/kg extends up to 8 km, the top of this isoline is at 6 km in Simulation1. This indicates that due to larger vertical velocities, the cloud water is transported to higher altitudes in Simulation2 than in Simulation1. The cloud ice content is significantly larger in Simulation1 (~0.4 g/kg maximum values) than in Simulation2 (~0.1 g/kg maximum values). In Simulation1, a secondary local maximum can be found at lower levels (between 5 and 6 km). This secondary peak in Simulation2 is absent. The higher amount of cloud ice in Simulation1 can be attributed to the fact that in that simulation, weaker updraft developed which resulted in smaller mean drop diameters. Then the smaller drops transported in sub-zero regions formed ice crystals instead of graupels.

The height of the 0 °C and –30 °C isotherms in *Fig. 13* inside the storms are similar in both cases (height of the 0 °C level is at ~3–4 km, the –30 °C level is at ~8 km). However, in Simulation2, the anomaly of these levels in the updraft region is somewhat larger than in Simulation1. This difference can be explained by the larger releasing latent heat of freezing and condensation in the case of Simulation2. More significant difference can be found if the shapes of the 15 °C isotherms are compared. The shape of this isotherm is affected by the latent heat of cooling due to melting and evaporation. A notable difference is, however, that the maximum of the height anomaly of this isotherm (reaching about several hundreds of meters and being slightly larger in Simulation2) is at the rear edge of the downdraft in Simulation2, while in Simulation1, it is located rather in the forward region of the downdraft.

Not only the intensity of updraft, but the strength of the downdraft is also strongly affected by the spatial resolution (*Figs. 13a* and *c*): the downdraft is more intense in Simulation2 than in Simulation1. The maximum value of downdraft is above 15 m/s in the case of Simulation2 and it is about 10 m/s in the case of Simulation1. Not only the maximum value of the downdraft is larger in the case of Simulation2, but the downdraft region is deeper, as well (~4 km versus ~3 km deep). The overlapping of the downdraft region, the height anomaly of the 15 °C isotherm, and the region where the graupel/hail mixing ratio is large suggest that the intensity of downdraft depends on the loading effect (represented by the sum of the mixing ratios of the precipitation elements – rain and graupel/hail particles) and on the cooling caused by the melting and evaporation of these species.

In order to identify the location and sources of the formation and growth of graupel/hail particles, production terms are plotted in *Fig. 14* in the same vertical cross sections as in *Fig. 13*. The following production terms are considered: (i) accretion of graupel/hail particles by rain drops; (ii) freezing of supercooled rain drops; (iii) freezing of supercooled rain drops due to the collision with cloud ice particles; (iv) riming of graupel/hail particles due collision with cloud drops; (v) collision between rain drops and snowflakes. The other sources, like evaporation/sublimation, snow-graupel/hail conversion through riming, and ice multiplication were found to be negligible comparing to the other, above mentioned terms (see *Fig. 15* for discussion). *Fig. 14* shows that most of the graupel/hail particles were formed in cloud volume between the altitudes of 3 km and 9 km. The vertical extension of this volume does not depend on the applied spatial resolution. Above and below that layer, the existence of graupel/hail is mainly due to the advection/convection and fall-out processes. The midlevel accretion rates of graupel/hail particles (*Figs. 14a* and *c*) by rain are similar in Simulation1 and Simulation2 ($\sim 10 \cdot 10^{-3}$ g/(kg·s)). However, the maximum of the riming rates of graupel/hail particles by cloud water (*Figs. 14a* and *c*) was significantly larger in the case of Simulation2 than in the case of Simulation1. ($\sim 15 \cdot 10^{-3}$ g/(kg·s) versus $\sim 10 \cdot 10^{-3}$ g/(kg·s)), which is a direct consequence of greater transport of cloud water by stronger updraft (refer to *Figs. 13b* and *d*). The larger amount of the rain between the melting level and the surface in Simulation2 (refer to *Fig. 13a* versus *Fig. 13c*) is the consequence of the melting of larger graupel/hail content. The collision between rain and snow much less efficiently produces graupel/hail particles than freezing of the rain drops. In Simulation2, it operates only in the right flank of the midlevel updraft, under the forward sheared anvil, where the snow begins to descend and can encounter to some amounts of rain. However, in the case of Simulation1, besides the anvil region, there is another and more significant maximum of this process in the updraft at around 7 km, as well.

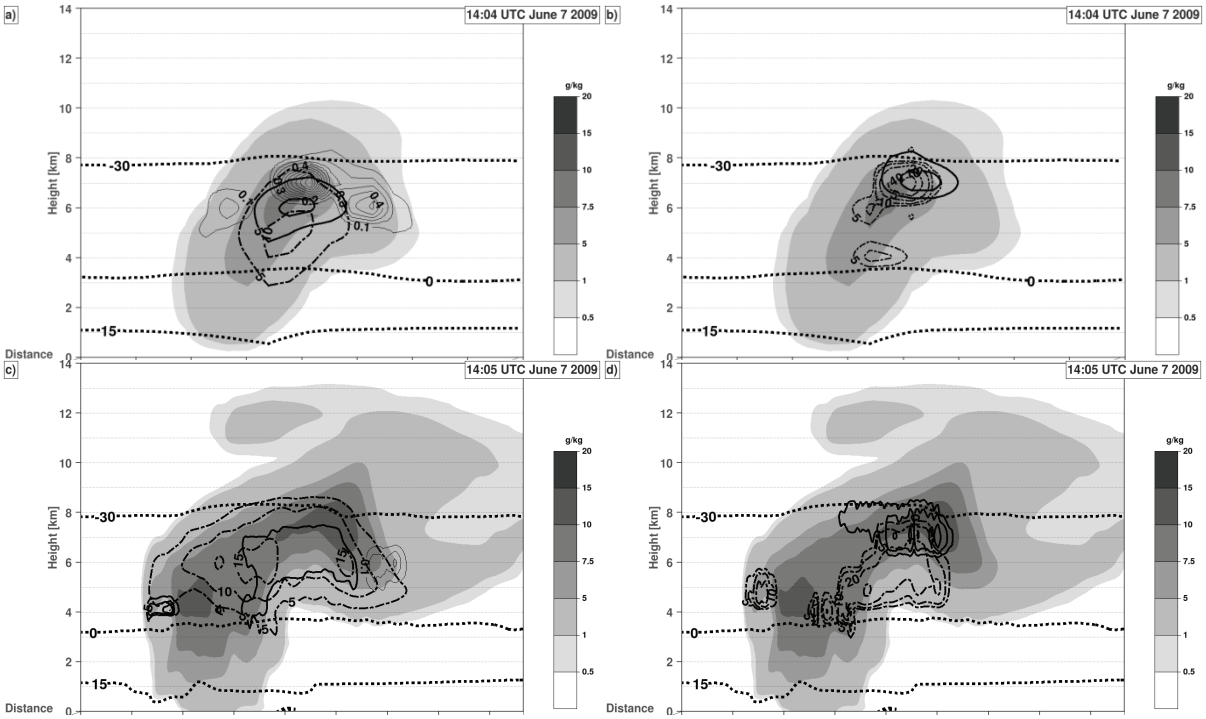

Fig. 14. Vertical cross sections of graupel production terms through the simulated thunderstorm on June 7, 2009 a) and b) in the case of Simulation1 at 14:04 UTC, c) and d) in the case of Simulation2 at 14:05 UTC. The orientation of cross sections is identical to the ones in *Fig. 13* (marked in *Fig. 9*). The displayed quantities are the followings:
a) and c) Shading represents the graupel mixing ratio (scale and legend are displayed in the pictures), thick solid lines show the values of production due to rain and graupel collision (contoured with intervals of $10 \cdot 10^{-3}$ g/(kg·s) and the minimum value is $5 \cdot 10^{-3}$ g/(kg·s)), the thick dot-dashed lines depict the accretion rate of cloud water by graupel (with contour intervals of $5 \cdot 10^{-3}$ g/(kg·s)), the light solid lines represent the collision between rain and snow (with contour intervals of $0.1 \cdot 10^{-3}$ g/(kg·s)) Thick dashed contours represent the isolines of 15, 0 and –30 °C.
b) and d) Shading represents the graupel mixing ratio (the scale and legend is displayed in the pictures), thick solid lines represent the freezing process of supercooled rainwater (contoured with intervals of $10 \cdot 10^{-3}$ g/(kg·s) and the minimum value is $5 \cdot 10^{-3}$ g/(kg·s)), the light dot-dashed lines show the production rate due to collision between rain and cloud ice (contoured with intervals of $10 \cdot 10^{-3}$ g/(kg·s), and the minimum value is $5 \cdot 10^{-3}$ g/(kg·s)). The thick dashed contours represent the isolines of 15, 0 and –30 °C.

The production rate by collision between supercooled rain drops and cloud ice particles (*Figs. 14b* and *d*) is two times smaller in the case of Simulation2 than in the case of Simulation1. This can be due to the larger cloud ice content aloft in Simulation1 (refer to *Fig. 13b*). A local maximum of this production rate can be also observed just above the melting level. This stems from the fact, that the ice crystals can form due to the break of the small ice fragments from the surface of the graupel/hail particles due to the collision between the graupel/hail particles and water drops (ice multiplication – *Hallet* and *Mossop*, 1974). The graupel/hail formation due to the freezing of the supercooled rain drops mostly occur in the region between the height of 6 and 8 km. The freezing rate is about two times larger in the case of Simulation2 than in the case of Simulation1 (~20–30·10^{-3} g/(kg·s) versus ~10–15·10^{-3} g/(kg·s)).

Time evolution of the volume integrated values of the above mentioned production terms were also investigated. The storm was divided into three volumes: (i) 8–14 km, (ii) 3–8 km, and (iii) 0 (surface) – 3 km. Production terms integrated over these volume characterize the microphysical processes in the low-, mid-, and upper-level parts of the storm. Results are summarized in *Fig. 15*. *Figs. 15a* and *b*, imply a clear evidence, that above $z = 8$ km, the graupel/hail mainly forms by the freezing of supercooled rain water and grows by collecting of supercooled cloud water. Another important process affecting the mixing ratio of graupel/hail is the transport by the vertical velocity (not shown) from lower elevations. Analysis of the plots in *Figs. 15a* and *b* shows that the sum of production terms integrated in time is much lesser than the graupel/hail mass formed in this volume, therefore, there has to be other sources than the productions of it. In the model, the only other source is the transport by convection. This confirms that besides the microphysical processes, the three-dimensional advection also plays important role in the evolution of the three dimensional structure of the graupel/hail particles. Due to the larger updraft in the case of Simulation2, significantly more graupel/hail particles can accumulate in the region above the height of 8km. The stronger convection of the cloud drops results in more efficient graupel/hail formation by freezing and larger riming rate as well.

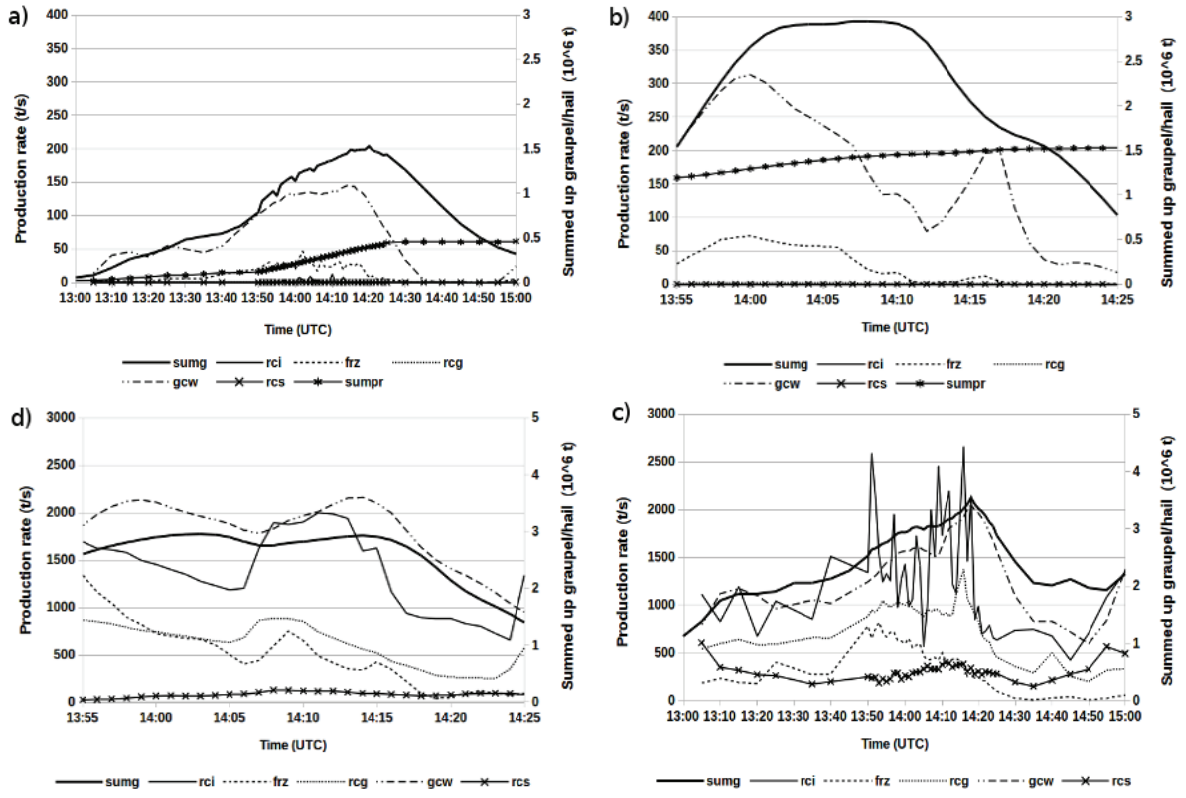

Fig. 15 a)-d). Time evolution of graupel production terms (in t/s), and graupel mass integrated over the volume of the storm a) between 8 and 14 km altitudes in the case of Simulation1, b) between 8 and 14 km altitudes in the case of Simulation2, c) between 3 and 8 km altitudes in the case of Simulation1, d) between 3 and 8km altitudes in the case of Simulation2. Abbreviations are the same as in *Figs. 10 c* and *d*. Curve sumg represents the total graupel content (in 10^6 t). While curve sumpr in a) and b) depicts the sum of all production terms integrated in time (in 10^6 t).

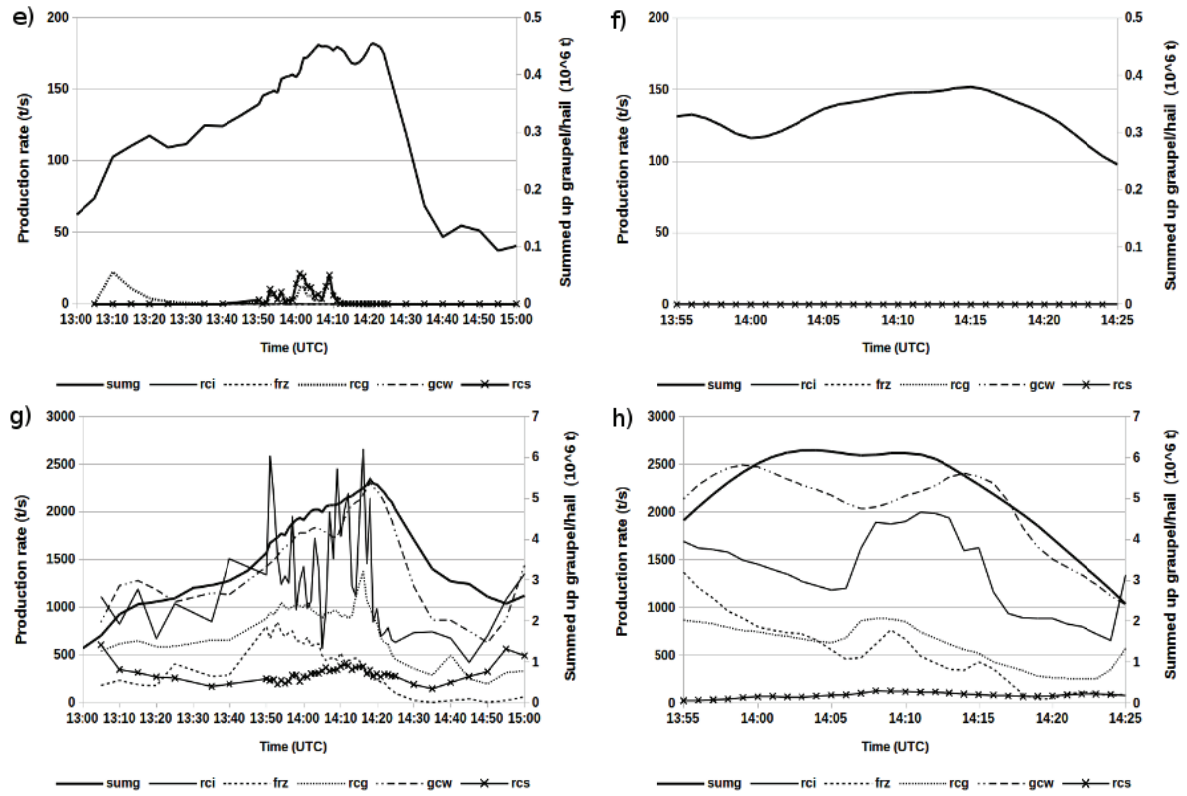

Fig. 15 e)-h). Time evolution of graupel production terms (in t/s), and graupel mass integrated over the volume of the storm e) between 3 km and the surface in the case of Simulation1, f) between 3 km and the surface in the case of Simulation2, g) over the whole column of the storm in the case of Simulation1, h) over the whole column of the storm in the case of Simulation2. Abbreviations are the same as in *Figs. 10 c* and *d*. Curve sumg represents the total graupel content (in 10^6 t).

Most of the graupel/hail content can be found in the middle region (between 3 and 8 km) in both cases (*Figs. 15c* and *d*). While the maximum of the graupel/hail mixing ratio was larger in the case of Simulation2 than in the case of Simulation1, the difference between the volume integrated values is nearly the opposite: the maximum of the volume integrated graupel/hail mass is between $3 \cdot 10^6$ and $4 \cdot 10^6$ T in Simulation1, while in Simulation2 it remains below $3 \cdot 10^6$ T during the Simulation. Most of graupel/hail particles formed by heterogeneous freezing of rain drops and freezing of supercooled rain drops due to collision with cloud ice. The latter process shows a rather hectic behavior with large jumps in intensity in Simulation1 with larger maximum than in Simulation2. This difference between the Simulations can be attributed to the greater cloud ice content in midlevels in Simulation1 (see again *Figs. 13b* and *d*). Formation of the graupel/hail particles was significantly affected by the horizontal resolution. As for the heterogeneous freezing of supercooled rain drops, Simulation2 produced similar rates as Simulation1. The amount of

graupel/hail formed by collision of snowflakes and rain drops was negligible in the case of Simulation2, however, in Simulation1, especially in the first minutes of the period, the snow-rain interaction played non-negligible role in creating graupel/hail (it even exceeds the production rate of the freezing of rain) and was more significant than in Simulation2 throughout the period. Subsequent growth of graupel/hail was largely driven by the accretion processes (accretion by cloud water and rain drops). In both simulations, accretion of graupel/hail by cloud water was more efficient than by rain water.

In the low-level region of the storm, below $z = 3$ km, which is the melting layer, positive values of graupel production are negligible according to *Figs. 15e* and *f*, and there is only one sink term: the sublimation of graupel particles. Production due to collision processes with rain and cloud drops is exactly zero, because in the melting region, all the liquid water amount collided with graupel particles is instantaneously shed to form rain drops. In the case of the total graupel/hail amount in this layer, Simulation1 exceeds the values of Simulation2 at the main part of the integration. This means that the cell in Simulation1 produced more graupel/hail at lower levels than its high-resolution counterpart, though this relation is not valid for the mean graupel/hail values at the surface according to the previous results (see *Fig. 12*). One explanation of this contradiction is that under a certain threshold of mixing ratio, all the graupel/hail particles melt during its falling. If this threshold is exceeded – this could be the case in Simulation2, where we found higher maximum values –, then there is some amount of solid particles which do not melt and, therefore, reach the surface. Based on these results, we can state that compared to its coarser counterpart, the finer resolution Simulation created a storm which produced higher low-level maximum values of graupel/hail mixing ratio but less total graupel/hail content than the storm simulated on the coarser resolution.

Figs. 15g and *h* shows that the total amount of graupel/hail formed in the whole cloud volume only slightly depends on the horizontal resolution ($6 \cdot 10^6$T in the case of Simulation2 versus $5.5 \cdot 10^6$ T in the case of Simulation1). In both cases, most of the graupel/hail particles formed by freezing of supercooled rain due to collision with cloud ice and due to heterogeneous freezing. In both Simulations, the first process is dominant over the second one. While in Simulation1 there is a non-negligible contribution to graupel/hail production by the rain-snow collision, this process has a negligible effect in the case of Simulation2. The graupel/hail particles subsequently grow by collision with cloud and rain water. The accretion by cloud water was more efficient than by rain water, in both simulations.

3.2.3. Results of the maximum hail size calculation method

According to Eqs. (4) and (6), the maximum size of the graupel/hail particles is a function of their mixing ratio. The shape of this function is similar to that of

the square root function (*Fig. 16*). This means that the value of the maximum hail size is more sensitive to the mixing ratio if the value of the mixing ratio is small, and near linearly increases with the mixing ratio above the value of 4 g/kg. Because Simulation1 and Simulation2 cases gave different amounts of graupel/hail on the surface (*Fig. 11*), the maximum hail sizes are expected to be also significantly different. Time evolutions of the largest maximum hail size on the surface are plotted in *Fig. 17*. The figure shows that the maximum hail size calculated by Simulation1 was less than 2 cm during most of the Simulation time; it increases above 2 cm only in a short time period of 10 minutes. However, the forecast maximum hail size in Simulation2 is above 3 cm almost throughout the whole time period and comes near to maximum value of 5 cm. According to the photo documentations and inflicted damages described in Section 3.2.1., the implemented hail size method yielded diameters closer to the observations in the case of Simulation2 than in the case of Simulation1.

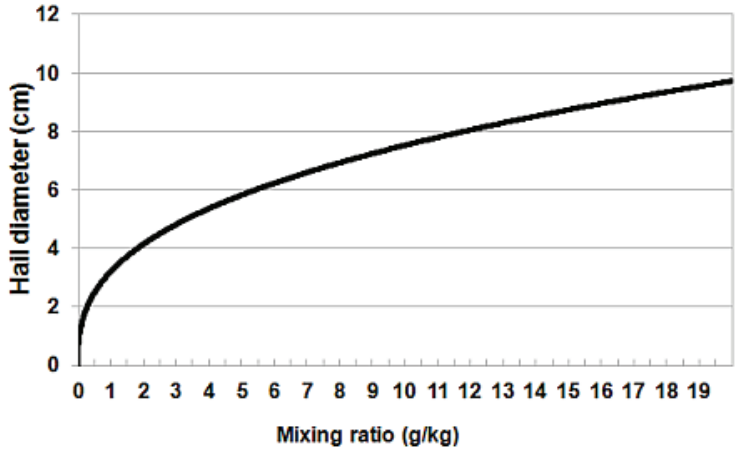

Fig. 16. The dependence of the hail size diameter (calculated by the method - cm) on the graupel mixing ratio (g/kg). The calculation was done in an environment of the following atmospheric conditions: T (temperature) = 25 °C, P (pressure) = 101000 Pa, r (water vapor mixing ratio) = 5 g/kg.

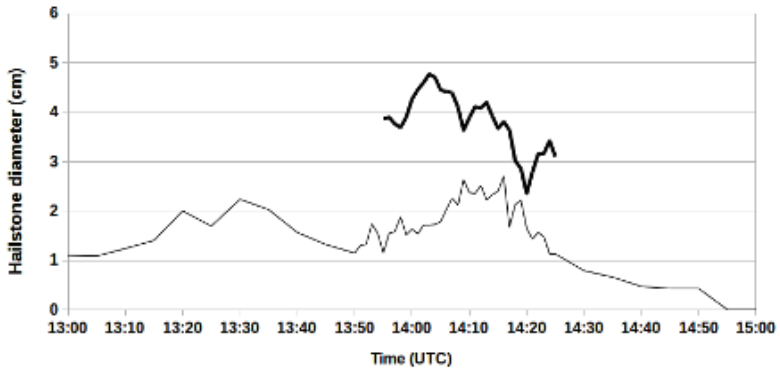

Fig. 17. Time evolution of the maximum hail size at the lowest model level. Light and thick solid lines denote the forecast maximum sizes in the case of Simulation1 and Simulation2, respectively. The units are cm (as diameters).

To illustrate the typical horizontal distribution of the expected hail sizes on the ground, horizontal cross sections of calculated hail sizes at the lowest model level are displayed at a given time in *Figs. 18a* and *b*. The maximum values in Simulation1 slightly exceeds 2.5 cm in one grid point which represents a 4 km^2 area. The maximum in-storm hail size in the finer simulation is above 4.5 cm on an area of roughly 1 km^2, and the isoline of 2.5 cm encloses an area of around 8 km^2, which is twice as high as in Simulation1. That is, the simulation with higher resolution resulted in not only larger maximum hail sizes, but the area exposed by these larger hail stones is also significantly larger in Simulation2 than in Simulation1.

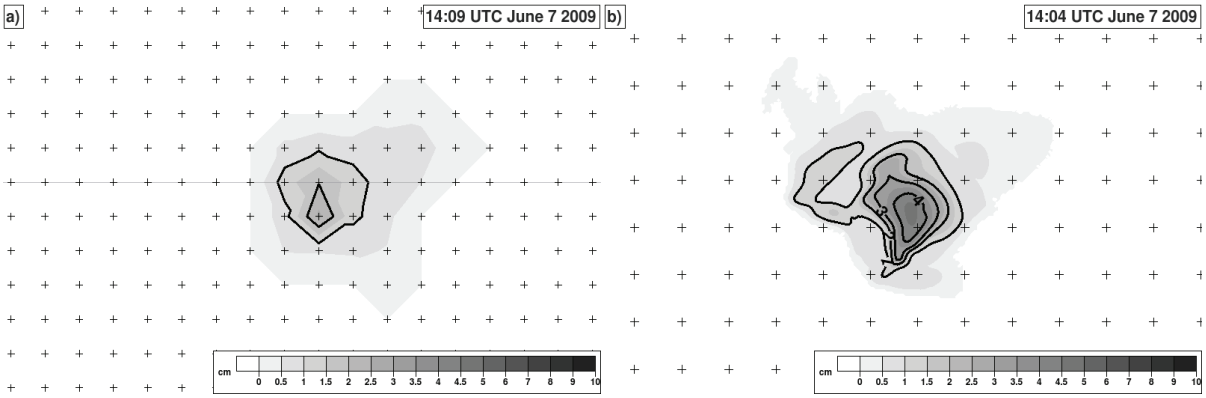

Fig. 18. Horizontal cross sections of the maximum hail sizes produced by the storm at the lowest model level a) Simulation1 at 14:09 UTC and b) Simulation2 at 14:04 UTC. The scale of the shading is as in the legend, its isolines are denoted by black solid lines. The distance between two neighboring crosses represents 2 km on both nests.

4. Summary and conclusion

In this paper, an algorithm was developed to evaluate a forecast method for the maximum hail size on the ground. The input data for this algorithm are given by WRF-ARW model with the Thompson's one-moment microphysical scheme, which treats graupel and hail as one hydrometeor category (graupel/hail). Besides that, a detailed analysis was made to reveal the dependence of microphysical processes (focusing on the graupel/hail formation and growth) on the horizontal resolution. The results were evaluated on two nests with horizontal resolution of 2 km (Simulation1) and 100 m (Simulation2). In order to better understand the mechanisms led to graupel/hail formation in the cloud, the production terms responsible for the graupel/hail formation and growth were also analyzed. A case study of a supercell produced large and damaging hail was selected to achieve these goals. Both Simulations were able to reproduce the main characteristics of the observed supercell, such as: radar reflectivity,

morphology, and vorticity fields. On the other hand, the details of these properties were significantly better simulated if the finer resolution was used.

The Simulation with finer resolution resulted in larger maximum values of graupel/hail and rain mixing ratios, but smaller maximum mixing ratios of cloud ice were calculated. The location of the maximum of graupel/hail mixing ratio was found in the updraft region between the heights of 5 and 8 km in both cases. The maximum values of cloud water and snow mixing ratio were found to be similar in both Simulations. Although the maximum of the graupel/hail mixing ratio was significantly larger in the case of Simulation2 than in the case of Simulation1, considering the total mass of graupel/hail particles in the storm, the two Simulations produced almost the same amount. The higher maximum values can be explained by the stronger updrafts occurred in the case of Simulation2. The stronger updraft resulted in more intense upward flux of water vapor, and it was able to held larger amount graupel/hail aloft. In addition, due to the stronger updraft in Simulation2, the maximum graupel/hail mixing ratio was located at higher altitudes than in Simulation1. The maximum of downdraft velocity was also larger in the case of Simulation2 due to the larger loading effect and cooling rate by melting and evaporation.

The graupel/hail in the storm formed mainly by the freezing of supercooled rain due to its collision with cloud ice, and secondly, by the heterogeneous freezing of supercooled rain. Nevertheless, the latter process was more intense in the finer Simulation than in its counterpart, while the rain-cloud ice collision at times was found more effective graupel/hail producer in Simulation1 than in Simulation2. This latter difference and the smaller maximum of graupel mixing ratio aloft, too, can be attributed to the larger amount of cloud ice remained in Simulation1, because the weaker updraft in that case produced smaller water drops which subsequently formed ice crystals instead of graupel particles. In addition, in the case of Simulation1, rain-snow collision resulted in significant amount of graupel/hail. The formed graupel/hail content subsequently grew mainly by the accretion by cloud water, and to a lesser extent, the accretion by rain water. However, the overall greater formation rate of graupel/hail resulted in more efficient accretion. The analysis of production terms in the various layers of the storm shows, that the most of the graupel/hail particles were formed between the height of 3 and 8 km, while above and below of this layer, the graupel/hail particles were mainly transported by the advection and by their fallout falling.

The application of both Simulations resulted in reasonable maximum hail size on the surface. However, significantly larger maximum hail size (around 4 cm) was forecast in the case of Simulation2 than in the case of Simulation1 (about 2 cm). In addition, the horizontal extent of the area with large hail size (above 2 cm) was about twice larger in the case of Simulation2than in the case of Simulation1.

The method for the forecast of maximum hail size can be applied not only in supercell cases but with ordinary and multicell storms, as well. Therefore, in the future, more case studies involving these types of storms must be elaborated to test the universal abilities of this method. In addition, numerical Simulation with other two-moment microphysics schemes (*Morrison et al*., 2005; *Milbrandt* and *Yau*, 2005; etc.) which allow greater degree of freedom on the size distribution should be performed to investigate their effect on the surface. Though the Simulation on the 100 m resolution nest was performed with applying a PBL scheme, it is necessary to clarify whether using a LES closure in that range ("terra incognita") would lead to consistent results.

References

Adlerman E.J., and *Droegemeier, K.K*., 2002: The sensitivity of numerically simulated cyclic mesocyclogenesis to variations in physical and computational parameters. *Mon. Weather Rev. 130*, 2671–2691.

Brimelow, J.C., Reuter, G.W., and *Poolman, E.P*., 2002: Modeling maximum hail size in Alberta thunderstorms. *Weather Forecast. 17*, 1048–1062.

Brimelow, C. and *Reuter, G.W.,* 2006: Spatial Forecasts of Maximum Hail Size Using Prognostic Model Soundings and HAILCAST. *Weather Forecast. 21*, 206–219.

Browning, K.A., 1968: The organization of severe local storms. *Weather 23*, 429–434.

Bryan, G.H., *Wyngaard, J.C.,* and *Fritsch, J.M*., 2003: Resolution requirements for the simulation of deep moist convection. *Mon. Weather Rev. 131*, 2394–2416.

Changnon, S.A., Pielke, R.A. Jr., Changnon D., Sylves, R.T., and *Pulwarty, R*., 2000: Human factors explain the increased losses from weather and climate extremes. *B. Am. Meteorol. Soc. 81*, 437–442.

Craig, C.G. and *Dörnbrack, A.,* 2008: Entrainment in cumulus clouds: What resolution is cloud-resolving? *J. Atmos. Sci. 65*, 3978–3988.

Ćurić, M., and *Janc, D.,* 1989: The behavior of a hailstone in a forced 1-D Cb cloud model. *Meteorol. Atmos. Phys.* 41, 45–54.

Ćurić, M., and *Janc, D.,* 1993: Predictive capability of a one-dimensional convective cloud model with forced lifting and a new entrainment formulation. *J. Appl. Meteorol. 32*, 1733–1740.

Doswell III, C.A., 1996: What is a supercell?. Preprints 18th Conf. Severe Local Storms (San Francisco, CA). Amer. Meteor. Soc, 641.

Farley, R.D. and *Orville, H.D*., 1986: Numerical Modeling of Hailstorms and Hailstone Growth. Part I: Preliminary Model Verification and Sensitivity Tests. *J. Climate Appl. Meteorol. 25*, 2014–2035.

Farley, R.D., 1987a: Numerical Modeling of Hailstorms and Hailstone Growth. Part II: The Role of Low-Density Riming Growth in Hag Production. *J. Clim. Appl. Meteorol. 26*, 234–254.

Farley, R.D., 1987b: Numerical Modeling of Hailstorms and Hailstone Growth. Part III: Simulation of an Alberta Hailstorm—Natural and Seeded Cases. *J. Clim. Appl. Meteorol. 26*, 789–812.

Fawbush, E.J., and *R.C. Miller,* 1953: A method of forecasting hailstone size at the earth's surface. *Bull. Amer. Meteorol. Soc. 34*, 235–244.

Fiori, E., Parodi, A., and *Siccardi, F*., 2010: Turbulence Closure Parameterization and Grid Spacing Effects in Simulated Supercell Storms. *J. Atmos. Sci. 67*, 3870–3890.

Geresdi, I., 1990: Two-dimensional simulation of a small hailstorm. *Időjárás 94*, 346–359.

Geresdi, I., 1996: Precipitation formation in a severe thunderstorm. *Atmos. Res. 41*, 71–81.

Geresdi, I., 1998: Idealized simulation of the Colorado hailstorm case: Comparison of bulk and detailed microphysics. *Atmos. Res*. *45*, 237–252.

Geresdi, I., Horváth, Á., and *Mátyus, Á.,* 2004: Nowcasting of the precipitation type Part II: Forecast of thunderstorms and hailstone size. *Időjárás 108*, 33–49.

Grabowski, W.W., Wu, X., Moncrieff, M.W., and *Hall, W.D.,* 1998: Cloud-resolving modeling of tropical cloud systems during phase III of GATE. Part II: Effects of resolution and the third spatial dimension. *J. Atmos. Sci. 55*, 3264–3282.

Grell, G.A., and *Dévényi, D.,* 2002: A generalized approach to parameterizing convection combining ensemble and data assimilation techniques. *Geophys. Res. Lett., 29(14),* Article 1693.

Hallett, J., and *Mossop, S.C.,* 1974: Production of secondary ice particles during the riming process, *Nature 249*, 26–28.

Horváth, Á. and *Geresdi, I.,* 2003: Severe storms and nowcasting in the Carpathian Basin. *Atmos. Res.*, *67–68*, 319–332.

Horváth, Á., Geresdi, I., Németh, P., Csirmaz, K., and *Dombai, F.,* 2009: Numerical modeling of severe convective storms occurring in the Carpathian Basin. *Atmos. Res*. *93*, 221–237.

Johnson, D.E., Wang, P.K., and *Straka, J.M.,* 1993: Numerical Simulations of the 2 August 1981 CCOPE Supercell Storm with and without Ice Microphysics. *J. Appl. Meteorol. 32*, 745–759.

Johnson, D.E., Wang, P.K., and *Straka, J.M.,* 1995: A study of microphysical processes in the 2 August 1981 CCOPE supercell storm. *Atmos. Res. 33*, 93–123.

Klemp, J.B., 1987: Dynamics of tornadic thunderstorms. *Annual Rev. Fluid Mech. 19*, 396–402.

Lemon, L.R., and *Doswell III, C.A.,* 1979: Severe thunderstorm evolution and mesocyclone structure as related to tornadogenesis. *Mon. Weather Rev. 107*, 1184–1197.

Mellor, G.L. and *Yamada, T*., 1982: Development of a turbulence closure model for geophysical fluid problems. *Rev. Geophys. Space Phys.*, 20, 851–875.

Milbrandt, J.A. and *Yau, M.K.,* 2005: A multimoment bulk microphysics parameterization. Part I: Analysis of the role of the spectral shape parameter. *J. Atmos. Sci. 62*, 3051–3064.

Milbrandt, J.A. and *Yau, M.K.,* 2006: A Multimoment Bulk Microphysics Parameterization. Part III: Control simulation of a Hailstorm. *J. Atmos. Sci. 63*, 3114–3136.

Miller, R.C., 1972: Notes on analysis and severe-storm forecasting procedures of the Air Force Global Weather Central. Air Weather Service Tech. Rep. 200 (Rev.), Air Weather Service, Scott Air Force Base, IL, 190 pp. [Available from Air Weather Service Technical Library, 859 Buchanan St., Scott AFB, IL 62225-5118.]

Moore, J.T. and *Pino, J.P.,* 1990: An interactive method for estimating maximum hailstone size from forecast soundings. *Weather Forecast. 5*, 508–526.

Morrison, H., Curry, J.A., and *Khvorostyanov, V.I.,* 2005: A new double-moment microphysics parameterization for application in cloud and climate models, Part I: Description. *J. Atmos. Sci. 62*, 1665–1677.

Ogura, Y., and *Takahashi, T.,* 1971: Numerical simulation of the life cycle of a thunderstorm cell. *Mon. Weather Rev. 99*, 895–911.

Orville H.D. and *Kopp, F.J.,* 1977: Numerical simulation of the Life History of a Hailstorm. *J. Atmos. Sci. 34*, 1596–1618.

Petch, J.C., Brown, A.R., and *Gray, M.E.B*., 2002: The impact of horizontal resolution on the simulations of convective development over land. *Q. J. Roy. Meteor. Soc. 128*, 2031–2044.

Putsay, M., Simon, A., Szenyán, I., Kerkmann, J., and *Horváth, Gy.,* 2011: Case study of the 20 May 2008 tornadic storm in Hungary — remote sensing features and NWP simulation. *Atmos. Res. 100*, 657–679.

Reisner, J., Rasmussen, R.M., and *Bruintjes, R.T.,* 1998: Explicit forecasting of supercooled liquid water in winter storms using the MM5 mesoscale model. *Q. J. Roy. Meteor. Soc*. *124*, 1071–1107.

Renick, J.H., and *Maxwell, J.B.,* 1977: Forecasting hailfall in Alberta. Hail: A Review of Hail Science and Hail Suppression, Meteor. Monogr., No. 38, Amer. Meteor. Soc., 145–151.

Simpson, J. and *Wiggert, V.,* 1969: Models of precipitating cumulus towers. *Mon. Weather Rev.* 97, 471–489.

Skamarock, W.C., Klemp, J.B., Dudhia, J., Gill, D.O., Barker, D.M., Duda, M.G., Huang, X.-Y., Wang, W., and *Powers, J.G*., 2008. A description of the advanced research WRF version 3. NCAR Technical Note NCAR/TN-475+STR, June 2008. 113.

Takahashi, T., 1976: Hail in an Axisymmetric Cloud Model. *J. Atmos. Sci. 33*, 1579–1601.

Talbot, C., Bou-Zeid, E., and *Smith, J.,* 2012: Nested Mesoscale Large-Eddy simulations with WRF: Performance in Real Test Cases. *J. Hydrometeor. 13*, 1421–1441.

Thompson, G., Rasmussen, R.M., and *Manning, K.*, 2004. Explicit forecasts of winter precipitation using an improved bulk microphysics scheme. Part-I: description and sensitivity analysis. *Mon. Weather Rev. 132*, 519–542.

Thompson, R.L., Edwards, R., Hart, J.A., Elmore, K.L., and *Markowski, P.*, 2003: Close proximity soundings within supercell environments obtained from the rapid update cycle. *Weather Forecast*. *18*, 1243–1261.

Weinstein, A.I., 1972: Ice-Phase Seeding Potential for Cumulus Cloud Modification in the Western United States. *J. Appl. Meteor. 11*, 202–210.

Wisner, C., Orville, H.D., and *Myers, C.,* 1972: A Numerical Model of a Hail-Bearing Cloud. *J. Atmos. Sci.*, *29*, 1160–1181.

Wyngaard, J.C., 2004: Toward numerical modeling in the ‘‘terra incognita’’. *J. Atmos. Sci*. *61*, 1816–1826.

Zoltán, Cs. and *Geresdi, I.,* 1984: A one-dimensional steady-state jet model for thunderclouds. *Időjárás 88*, 21–31.